



Size-Wise Effect of Agricultural By-Product-Derived Calcium Phosphate Composites on Stem Cell Osteogenesis

Kyoung-Je Jang^{1,2} · Sangbae Park^{3,4,5} · Juo Lee^{6,7} · Yeonggeol Hong¹ · Hoon Seonwoo^{7,8} · Ki-Taek Lim⁹ · Jangho Kim^{3,4,5} · Jong Hoon Chung^{10,11,12}

Received: 20 March 2023 / Revised: 12 September 2023 / Accepted: 13 September 2023
© The Author(s), under exclusive licence to The Korean Society for Agricultural Machinery 2023

Abstract

Introduction Collagen and other natural polymers including hyaluronic acid and chitosan (CS) are common additives for improving the bone forming capacity and retain the structures of xenografts. The topography of the cell-attaching region on implants has a significant role in the cell behavior. To control the topography of calcium phosphate composites (CPCs) in the cell-attaching regions, equine bone powders (EBPs) with various sizes and CS solutions were used to fabricate CPCs. A correlation between the particle size distribution of the equine bone-derived calcium phosphate composites (EB-CPCs) and behavior of mesenchymal stem cells was observed. The EBPs were classified according to the granule size. The main crystal was hydroxyapatite.

Results The results of the surface roughness measurements revealed that in the groups containing hydroxyapatite particles with sizes of 5 μm , 50 μm , and 100 μm , the R_z values were 23.199, 43.274, and 69.701 μm , respectively. The ultimate compressive strengths for the groups with hydroxyapatite sizes of 5 μm , 50 μm , and 100 μm were 1.98 ± 0.058 MPa, 1.36 ± 0.17 MPa, and 1.96 ± 0.14 MPa, respectively. A cell viability analysis revealed that a higher R_z led to elongated shape, resulting in an enhanced cell proliferation. A lower R_z led to rounded shape, resulting in an increased osteogenic differentiation.

Conclusion In conclusion, control of the powder particle size in the fabrication of CPCs is an important factor affecting osteogenesis.

Keywords Equine bone powders · Particle size · Calcium phosphate composite · Surface roughness · Osteogenesis

Introduction

Owing to the aging society and increase in leisure time including sport activities, there is an increasing number of patients suffering from bony defects (Giannoudis et al., 2005; Kim et al., 2019). Three techniques are used to treat bone defects: autograft, allograft, and xenograft techniques. The method of autografts, based on extraction of a patient's normal spongy bone, has the best recovery among all methods (Mahendra & Maclean, 2007). In the allograft method, donated bone is implanted into wounded area, while that of xenograft is based on bone implantation between the heterogeneous such as horse and human. The autograft and allograft methods are generally preferred to avoid the risk of

immune response. However, due to several limitations, such as the need for an additional surgery (Mahendra & Maclean, 2007), lack of donors, and possibility of infection (Hofmann et al., 1995), the xenograft method is commonly used to regenerate bone defects. Furthermore, xenografts have better osteoconductivity and osteoinductivity than alloplasts because they implant synthesized hydroxyapatite (HA) or tricalcium phosphate. HA serves as the primary crystalline structure in animal bones, with a Ca/P molar ratio of 1.67, meaning that there is no significant variation in the Ca/P ratio due to HA. Notably, the actual Ca/P ratio of the animal bone mineral is between 1.37 and 1.87 because there are some trace elements, including Sr, Mg, Zn, Si, and Co. Ca/P stands for Calcium to Phosphorus ratio. The variability of the Ca/P ratio across various calcium phosphate compounds is a crucial factor influencing their properties and roles in biological systems. This ratio holds considerable significance in influencing osteogenesis and the process of bone

Kyoung-Je Jang and Sangbae Park contributed equally to the work.

Extended author information available on the last page of the article

formation. Therefore, maintaining an appropriate Ca/P ratio is crucial for bone formation and osteogenesis, as it contributes to the creation and maintenance of healthy bone tissue. The existence of trace elements in HA crystals influences their crystalline and physicochemical structures (Jang et al., 2014), which significantly affect biological behaviors when these materials are used as implants (Akram et al., 2014; Mucalo & Worth, 2008). In this regard, an exogenous bone has a better healing capacity than synthetic orthophosphates. Source of these exogenous bone includes bovine and porcine bones, which are common agricultural by-products. Their utilization drastically curtails both production cost and disposal expenses. The most common exogenous bone sources for clinical use are bovine and porcine bones. However, there have been limited studies on deproteinized equine bones. In our previous research, when using equine bone as a heterogeneous bone material in calcium phosphate cement (CPC), we confirmed that CPC derived from equine bone exhibits superior cell viability in interactions with cells (Jang et al., 2021). This implies that when used as a graft material, transplanted tissues or cells may better maintain their viability. Furthermore, equine bone-based CPC may be associated with lower or negligible immune reactions compared to heterogeneous bone materials from other animal species. This suggests that the transplanted tissue or material is less likely to provoke a response in the host animal's immune system, reducing the risk of transplant rejection. This aids in the successful integration of the transplanted material and promotes tissue formation.

There have been many attempts to improve the bone forming capacity of xenografts using collagen with a calcium phosphate powder and exogenous bone (Salamanca et al., 2018). Other natural and synthetic polymers are also in use of improving the bone forming capacity and retain the structure (Lim et al., 2020; Park et al., 2021). Typical methods used to fabricate calcium phosphate composites (CPCs) include mixing of a calcium orthophosphate powder with solutions such as poly(methyl methacrylate) (PMMA) or other polymeric solutions. However, the polymerization of PMMA generates temperatures high above 100 °C that necrosis of tissues surrounding the implant region is resulted (Böker et al., 1989). To overcome this limitation, chitosan (Xu et al., 2002), gelatin (Bigi et al., 2004), hyaluronic acid (Alkhraisat et al., 2009), and citric acid (Barralet et al., 2005) can be dissolved in liquids to enhance the solubility of calcium (Ca) or phosphorus (P) ions, as demonstrated in previous research. Among these, chitosan stands out as a biocompatible biomaterial with high biodegradability. This implies that chitosan combined with CPC gradually degrades over time, safely disappearing from the treatment area. Hence, the research was aimed at enhancing the mechanical strength of CPCs. To improve the mechanical strength, control of powder particle size has been extensively

studied for the purpose. Variation in particle size of CPCs influences its ion solubility, setting time, porosity, and compressive strength, which in turn affects its biocompatibility, bioactivity, and bone recovery. (Ambrosio et al., 2012; Shi et al., 2009; Zhou & Lee, 2011) It is hypothesized that size-wise distribution CPCs particles would change its surface topography (Bigerelle et al., 2002; Jang et al., 2021). The surface topography at cell-attaching site has a crucial role in the cell behavior. Characteristics of cell-attached regions affect the cell morphology and subsequently determine the cell fate (Bettinger et al., 2009). Therefore, the control of the surface topography of CPCs can affect the morphology, cellular function, and fate of attached cells. Relevant recent studies on particle size distribution generally target on the mechanical properties and solubility of CPCs. However, there are limited studies on the interaction between surface topography of CPCs and cellular behavior.

In this study, a relationship between cell behavior and the equine bone-derived CPCs (EB-CPCs) with various particle size was investigated. EB and CS composites were fabricated using equine bone powders with various particle sizes and CS solutions. CPC-chitosan composites can exhibit the ability to harden rapidly within a short period (Xu et al., 2004). Their morphologies were observed via field-emission scanning electron microscopy (FE-SEM). The surface topography was then quantitatively assessed. Criteria including cell behavior, viability, adhesion, and osteogenesis of CPCs were assessed to verify interactions between the particle size distribution and cell behavior.

Materials and Methods

Preparation of Equine Bone Powders

EBs (Baekma Garden, Jeju-do, South Korea) were contained in tap water for 2 h to wash out blood. This step was repeated 3–4 times. The EBs were then immersed in hydrogen peroxide in a ratio of 3:1 (v/v) for 48 h, followed by removal of the flesh out of the bones. The EBs were then dried for 48 h. The raw source was placed in an alumina crucible ($10 \times 10 \times 20 \text{ mm}^3$) and sintered in an electrical furnace at 600 °C for 2 h. The sintered EBs were then broken into pieces smaller than 2 mm in size using a mortar and pestle to create a coarse powder. The EB powder was placed in the alumina crucible and sintered at 1300 °C for 10 h. Sintered EB powders (EBPs) were prepared via two different types of milling. Sintered EBs were ground by an impact mill (A10, IKA, Germany) for 1 min. To separate particles according to size, woven wire sieves were used, including 325-, 270-, 250-, 150-, and 115-mesh structures. Some parts of the ground EB powder that passed through the 325-mesh woven sieve were ground by an air jet mill (MHK Trading

Company, Republic of Korea). After sieving, three samples were chosen between the 270 and 250-mesh sieves (50 μm) and between the 150- and 115-mesh sieves (100 μm) and ground with an air jet mill. The particle size of each sample was then measured by a dynamic light scattering analyzer (Malvern, Master Sizer S, USA).

Fabrication of EB-CPCs

CS powder (YB BIO Cooperation, Republic of Korea), 94% deacetylation, and 2% (v/v) lactic acid solution were used for a preparation of CS solution. A beaker was filled with 490 mL of distilled water, and then 10 mL of lactic acid was added. To the 2% lactic acid solution prepared, 17.5 g of the CS powder was added, and the solution was stirred for 24 h at 120 rpm. Subsequently, the CS solution was filtered via the filter paper method. EB and CS cements (EB/CS) were fabricated following the previous methods (Jang et al., 2021). The ratio between powder and liquid in the mixture was 1 g to 0.5 mL. Upon mixing, a calcium phosphate paste was injected into a Teflon mold (6 mm (diameter) \times 12 mm (height)). The Teflon molds with the calcium phosphate paste were set for 48 h at 37 °C and humidity of 98%. The experimental groups were defined as follows: a composite of 5 μm EBP and CS solution (EB/CS-5), a composite of 50 μm EBP and CS solution (EB/CS-50), and a composite of 100 μm EBP and CS solution (EB/CS-100).

Characterization of EB-CPCs

Functional groups of the EBP were investigated to identify the presence of anions partially substituting PO_4^{3-} and OH^- groups and residues of organic compounds. Fourier-transform infrared (FT-IR) spectrometry (Nicolet 6700, Thermo Scientific, USA) was used to measure the infrared spectra of the samples in the range of 4000–650 cm^{-1} with a resolution of 8 cm^{-1} . The crystal structures of the sintered EBPs and other reference materials were analyzed via X-ray diffractometry (XRD; D8 ADVANCE with DAVINCI, Bruker, Germany) with Cu K_α radiation ($\lambda=0.154$ nm) at 40 kV and 40 mA. Scans were obtained in 2θ range of 20 to 60° at 1°/min. An X-ray fluorescence (XRF) analysis of the bone powder and the rest was performed using a wavelength-dispersive (WD) XRF spectrometer S4 Pioneer (Bruker, AXS, Germany) equipped with a Rh X-ray tube (4 kW). The compressive strength of EB/CS was measured using a texture analyzer (TA.XT, Stable Micro Systems, UK). After hardening for 48 h, hardened EB/CSs with dimensions of 6 mm in diameter and 12 mm in height were prepared. The compressive stress on samples was monitored at a loading rate of 0.01 mm/s using a stainless 6-mm cylindrical probe. A surface roughness analyzer (Surftest SJ-410, Mitutoyo America Corporation, USA) with a diamond tip with a

radius of 2 μm and cone angle of 60° was used to obtain the surface roughness of the EB/CSs. The roughnesses of the samples were measured according to International Organization for Standardization (ISO) 1997 with a range of 8 μm , measuring speed of 0.05 mm/s, measuring force of 0.75 mN, and total measuring length of 2.5 mm. Five measurements were collected in each sample group.

In-vitro Study

To quantitatively evaluate the cell proliferation rate with EB/CSs, human alveolar bone marrow stem cells (hABMSCs) were cultured on EB/CSs. These cells were cultured for 7 days with α -minimum essential medium (α -MEM) proliferation media supplemented with 10% fetal bovine serum (Cytiva, US) and 1% antibiotics at 37 °C under 5% CO_2 conditions. The cell morphology was monitored by field-emission scanning electron microscopy (FE-SEM, Supra 55VP, Carl Zeiss, Germany). Three days after seeding, 4% paraformaldehyde was used to fix each sample for 30 min. A modified Karnovsky's fixative solution was added to the sample for 2 h at 4 °C for the primary fixation. The samples were then rinsed with 0.05 M of a sodium cacodylate buffer three times for 10 min at 4 °C, followed by immersing them into a 1% osmium tetroxide solution for 2 h. The samples were then gently rinsed twice using distilled water at room temperature. Subsequently, the samples were dehydrated by ethanol of ascending purity, 30, 50, 70, 80, 90, and 100%, for 10 min. The samples were then contained in hexamethyldisilazane for 15 min, twice, to dry. The FE-SEM observation was conducted using a FE-SEM.

The cell proliferation was assessed using a WST-1 cell viability assay kit (EZ3000, Daeillab Service Co., Republic of Korea). In the given test, samples were treated with a culture medium containing 10% WST-1 solution at 1, 3, and 7 days after cell seeding. After 2 h of incubation at 37 °C and humidity of 5%, all mixing media were transferred into microtubes, followed by centrifugation to precipitate residues of the samples. The supernatant from the extraction media was transferred to 96-well plate. The optical density of each sample was measured by a microplate reader (Tecan, Switzerland).

To evaluate the osteogenic capabilities of the EB-CPCs, EB/CSs were fabricated as circular plates with 6 mm in diameter and 2 mm in height. The hABMSCs were seeded on the CPC at 1×10^6 cells/mL of proliferation medium for 24 h. Osteogenic media were used to evaluate the osteogenic behavior of the cells. The media were freshly replaced every 2 days. Composition of the osteogenic medium is α -MEM supplemented with 10% fetal bovine serum, 1% antibiotics, ascorbic acid, β -glycerophosphate, and dexamethasone. For calcium mineral deposition assessment, alizarin red staining was performed with cells cultured on EB/CSs for 2 and

3 weeks. The samples were rinsed twice with phosphate-buffered saline (PBS), fixed with 4% paraformaldehyde, rinsed three times with PBS, and stained with an alizarin red S solution for 30 min under room conditions. Specimens were then destained with cethylpyridium chloride, and de-stained solutions were transferred to a 96-well plate for measuring absorbance at 570 nm using a microplate reader.

Statistical Data Analysis

All quantitative data are presented as mean \pm standard deviation. A statistical analysis was carried out using *R* for Windows v3.4.3 (www.r-project.org). An analysis of variance was carried out to analyze differences among multiple groups, followed by Duncan's multiple range test for a post hoc analysis. The level of significance was set at $p < 0.01$.

Results and Discussion

Powder Characterization

Figure 1A shows the morphologies of the EBPs with various sizes. The particle size changes assuming that the

classification of EBPs by particle size was successfully accomplished. In particular, 5 μm EBPs was larger than 10 μm , likely due to aggregation during air jet milling. A quantitative study was carried out to measure the particle size. The particle size distribution of EBPs post milling process is shown in Fig. 1B. The graph of the 5 μm EBPs first reached 100%, which indicates that the particles in the 5 μm EBPs contained more small particles than the other EBPs. 50 μm EBPs contained more particles with diameters above 30 μm than the 5 μm EBPs. The 100 μm EBPs was mainly composed of particles with diameters above 100 μm . Figure 1C shows quantitative data of each EBP expressed by *D* values (D10, D50, and D90). The *D* value indicates the particle size that corresponds to the mass fraction of the whole sample. The diameter D10 indicates the particle size to mass ratio of 10:90 (summation under D10:summation over D10). The *D* values of the EBPs are presented in Fig. 1B, which shows that each EBP was well divided. Figure 2A shows characteristic bands of the synthesized HA and sintered EBP separated by particle size. HA is composed of PO_4^{3-} , OH^- , and Ca^{2+} . FTIR spectroscopy may identify the existence of PO_4^{3-} , which has characteristic bands at 1090, 1052, and 963 cm^{-1} . In this study, the synthesized HA and EBPs have PO_4^{3-} adsorption band peaks at 1090, 1052, and 963 cm^{-1} .

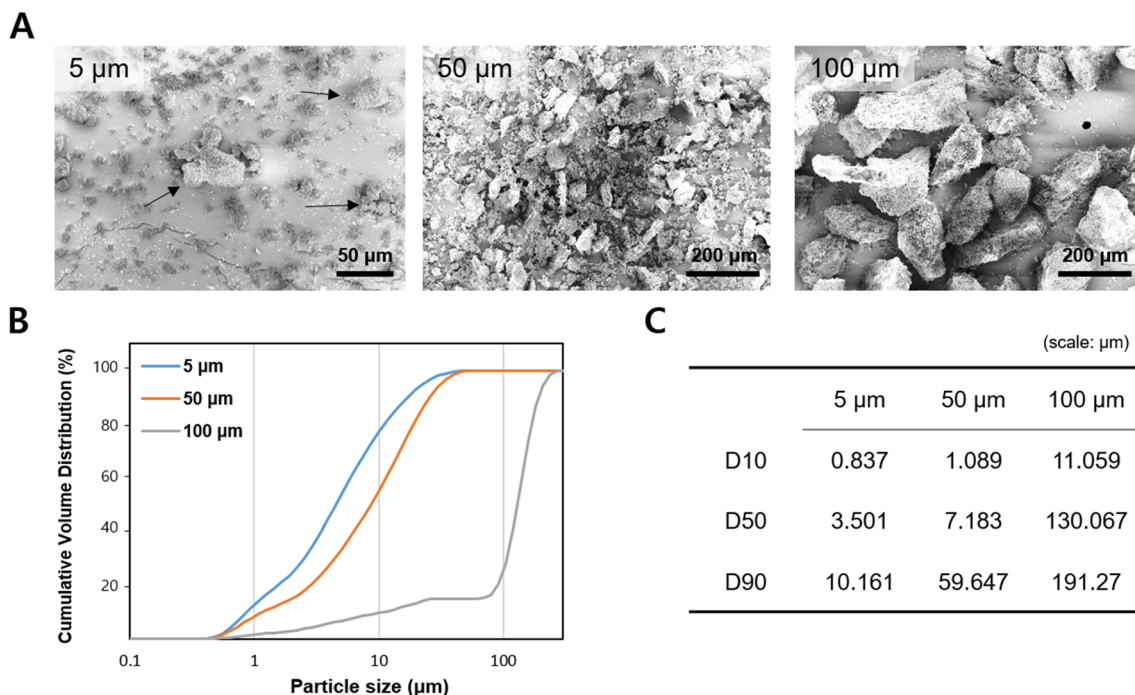


Fig. 1 Characteristics of equine bone powders (EBPs) according to particle size. **A** FE-SEM images of prepared EBPs. Image of 5 μm EBPs shows aggregated small granules under 5 μm (arrow represents aggregated particles). Image of 50 μm EBPs shows EBP granule size between 50 and 100 μm . Image of 100 μm EBPs shows EBP granules above 100 μm . **B** Cumulative particle size distribution of EBPs. Blue line indicates particle distribution of 5 μm EBPs with over 80%

EBPs smaller than 10 μm . Orange line indicates particle distribution of 50 μm EBPs with over 50% EBPs smaller than 10 μm . Gray line indicates particle distribution of 100 μm EBPs with over 80% EBPs smaller than 100 μm . EBPs above 80% are larger than 100 μm . **C** Table of particle size distribution analysis of EBPs according to volume median diameter of D10, D50, and D90

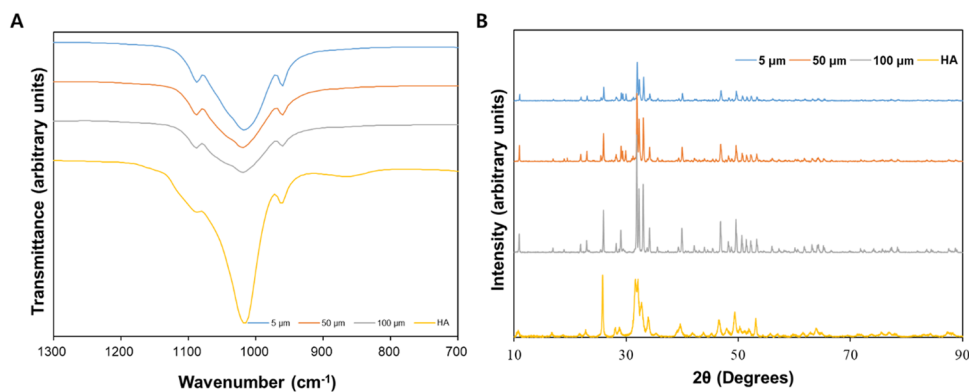


Fig. 2 Characterization data of EBPs via FT-IR and XRD. **A** FT-IR spectra of heat-treated EBPs with various particle sizes and synthetic HA. Each sample shows spectrum of PO_4^{3-} . **B** X-ray diffraction patterns of EBPs with various particle sizes and synthetic HA. Each sample has peaks at the same degrees, indicating that their crystal

structures are the same. However, the characteristic bands of EBPs are narrower than those of synthetic HA, indicating that EBPs are larger than synthesized HA. This is likely due to fusion of crystals in equine bone during heat treatment, resulting in larger crystals than natural crystals

An XRD analysis of the samples is presented in Fig. 2B. The XRD patterns of the EBPs have narrower peaks than the synthesized HA samples because larger crystals have narrower peaks than smaller crystals. In addition, the intensities of the characteristic peaks decreased as the particle size decreased, which indicates that HA crystals split as the particle size decreased. According to the FTIR spectroscopy and XRD results, the presence of HA as the main crystal was confirmed in all EBPs. Furthermore, we utilized X-ray Photoelectron Spectroscopy (XPS) to analyze the differences among each sample. XPS, known as Electron Spectroscopy for Chemical Analysis (ESCA), is a technique used for elemental and chemical analysis of surfaces. Peaks corresponding to C, O, P, and Ca were identified, and their relative ratios were determined. The analysis results did not reveal any significant differences among the samples (Figure S1).

Characterization of EB-CPCs According to Particle Size

After evaluation of EBP characteristics, EB-CPCs were fabricated with each powder. Top-view FE-SEM images are shown in Fig. 3A. The FE-SEM results revealed that the different surface morphological features differ according to the particle size. EB/CS-100 had more pores and fewer uniform surfaces than the other samples (Fig. 3A). Contour maps of each specimen were obtained using confocal laser scanning microscopy (CLSM) to support the FE-SEM observations. Blue regions in the maps indicate lower altitudes, while red regions indicate higher altitudes. The EB-CPCs obtained with larger particles led to higher differences in altitude. To evaluate numerical topographical differences of each EB-CPC, the surface roughness was measured by a surface roughness analyzer. Figure 3B shows the surface

roughness results. R_z was calculated by the averaging the five highest and five lowest values. The R_z values of EB/CS-5, EB/CS-50, and EB/CS-100 were 23.199, 43.274, and 69.701 μm , respectively, which indicate that cements obtained with larger EBPs have higher R_z values. These results indicate that EB/CS-100 has the roughest surfaces among all samples. Upon the mixing with the CS solution, EBPs were packed, and gaps could be generated between particles. Because EB/CS-100 has larger EBPs than EB/CS-5 and EB/CS-50, the probe of the roughness test machine can recognize gaps and particles. Therefore, R_z of EB/CS-100 may be highest among the samples.

The surface characteristics of cell-attaching regions have a profound impact on cellular behavior (Abagnale et al., 2015; Biggs et al., 2009; Clark et al., 1990). Therefore, the surface topography of EB-CPCs is expected to affect the behaviors of attached cells. For a clinical use of EB-CPCs, sufficient compressive strength is required for enduring compressive forces. Therefore, the compressive strengths of the EB-CPCs were analyzed (Fig. 3C). The ultimate compressive strengths of EB/CS-5, EB/CS-50, and EB/CS-100 were 1.98 ± 0.058 , 1.36 ± 0.17 , and 1.96 ± 0.14 MPa, respectively. EB/CS-5 and EB/CS-100 were stronger than EB/CS-50. After mixing of EBPs and CS solution, the mixed pastes had different mobilities, although their masses were the same, owing to the different surface areas attributed to the various sizes of the EBPs, which affected the interactions between the EBPs and CS solution. In the case of EB/CS-100, a sufficient interaction was assumed between the EBP and CS solution. Therefore, EB/CS-5 had the same ultimate compressive strength as that of EB/CS-100. For EB/CS-50, an improper interaction was assumed between the EBP and CS solution because of the ratio of powder to solution. In the case of EB/CS-5, a lack of interaction was assumed between the EBP

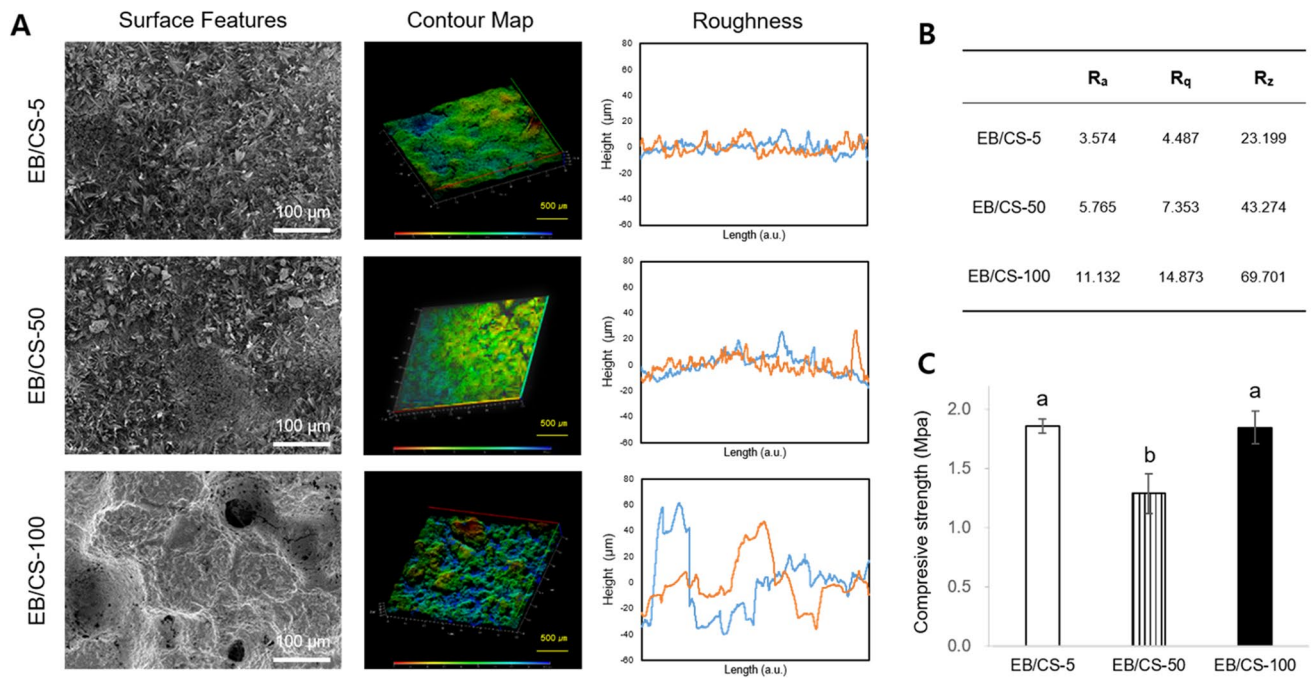


Fig. 3 Characteristics of EB/CS composites. **A** Left column is FE-SEM images of EB/CS composites (Top: 5 μ m EB, Middle: 50 μ m EB, Bottom: 100 μ m EB). Middle column is CLSM images exhibiting surface roughness of EB-CPCs. Colors in CLSM images indicate heights of surfaces and graph shows surface height (each line color indicates repetition test). Right column is result of surface roughness tester (Top: 5 μ m EB, Middle: 50 μ m EB, Bottom:

100 μ m EB). Each line indicates result of each test. **B** Surface roughness results of EB/CS composites with various EB powder sizes. R_a denotes the average surface roughness, R_q signifies the root mean square roughness, and R_z represents the distance between the highest and lowest points on the surface. **C** Compressive strength of EB/CS composites with various EB powder sizes ($n=5$, $p<0.01$). Error bars indicate standard deviation

and CS, but the smaller particles were more densely packed than the large particles. For these reasons, in the cases of EB/CS-5 and EB/CS-50, the observed aggregation among EBPs led to no discernible differences between the groups (Fig. 4A). However, it can be confirmed that the experimental results align with our hypothesis, as smaller EBP sizes indeed resulted in lower surface roughness in EB/CS, while larger EBP sizes led to higher roughness values. The results of the roughness test prove this speculation. This phenomenon validates the hypothesis that CPC surface roughness can be controlled by the particle size of EBP. Additionally, one of the reasons for the CPC surface becoming smoother when using small HA particles could be attributed to the reduction in CPC porosity through mineralization as CPC particles become smaller. In fact, we observed a decrease in surface porosity of CPC when MC3T3-E1 cells were cultured on the CPC (Figure S2).

In-vitro Study

After the characterization of the EB-CPCs, their in-vitro properties were investigated. As mentioned, the surface topography at cell-attaching site has a crucial role in the cell behavior. In particular, the cellular morphology is strongly

influenced by changes in surface topography. Therefore, we investigated the cellular morphologies of hABMSCs according to the EB-CPC group. Figure 4A shows FE-SEM images of hABMSCs cultured on each EB-CPC. Their lengths were measured using the software ImageJ. Major and minor axis lengths were calculated from ellipse looking structure of single cell (Fig. 4A). The cells cultured with higher R_z values had more elliptical shapes. Conversely, cells cultured with lower R_z values were closer to rounded shape (Fig. 4B–D). Cell viability results are shown in Fig. 4E. The cell viability of the EB/CS-100 group was markedly increased compared to the other groups. However, insignificant differences in cell viability were observed between EB/CS-5 and EB/CS-50. Until the third day, there was a significant similarity in cell viability between EB/CS-50 and EB/CS-100. However, upon observing cell viability on the seventh day, while other groups displayed a general decrease in cell viability, EB/CS-100 showed a slight increase. This phenomenon implies that EB/CS-100 is less influenced by fundamental factors or processes affecting cell survival or proliferation over time compared to other groups. The decrease in cell viability observed in the other groups may be attributed to a relative reduction in cell proliferation as osteogenic differentiation progresses in the EB/CS-5 and EB/CS-50 groups

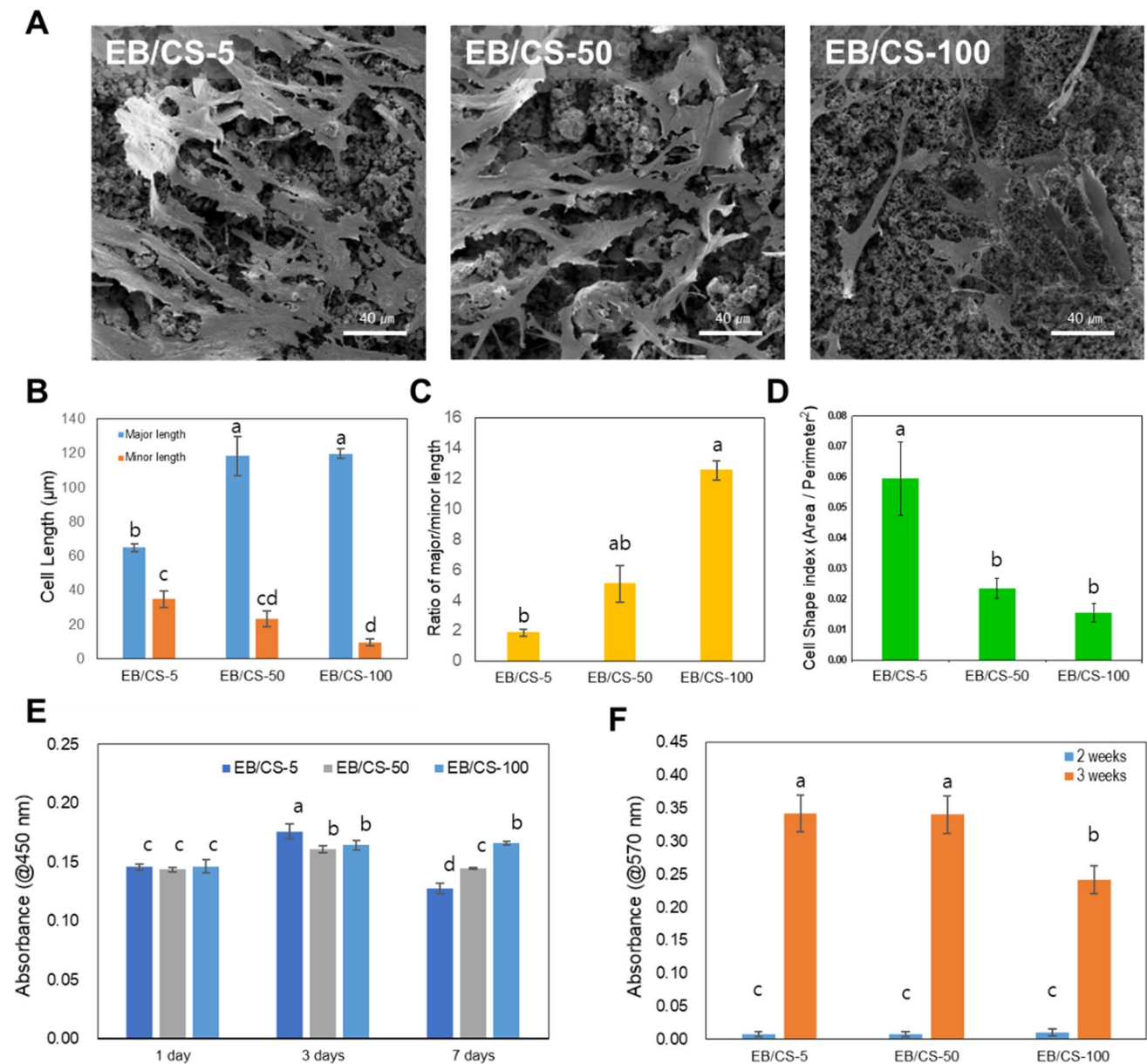


Fig. 4 Results of cellular behavior on EB/CS composites. **A** FE-SEM images of hABMSCs on EB/CS composites (3 days). **B** Analysis of cellular morphologies using ImageJ software via FE-SEM images ($n=5$, $p<0.01$). **C** Major/minor axis ratios of hABMSC on EB-CPCs. Cells on EB/CS-100 are longer than others ($n=5$, $p<0.01$). **D** Cell shape index (area)/(perimeter)² ratios of hABMSC on EB-

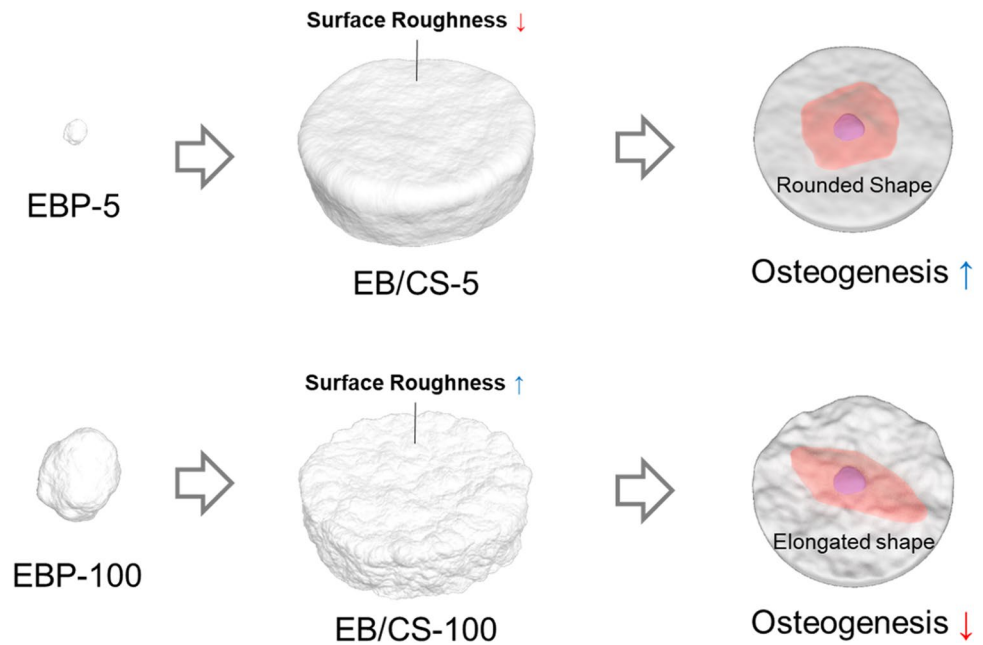
CPCs. Cells on EB/CS-100 are longer than others ($n=5$, $p<0.01$). **E** Cell viability results of hABMSC on EB/CS composites with WST-1 assay for 7 days. On day 7, there were significant differences with each EB-CPC ($n=5$, $p<0.01$). **F** Alizarin red staining results of each EB-CPC group ($n=5$, $p<0.01$). Error bars indicate standard deviation

(Ruijtenberg & van den Heuvel, 2016). Consequently, the cell proliferation was highly stimulated on the surface of EB/CS-100, likely due to the promotion of the cell-attaching region of EB/CS-100 enhancing the cell attachment and proliferation.

Alizarin red staining was performed to investigate the osteogenic capabilities of the EB-CPCs (Fig. 4F). At week 2, the optical densities of all EB-CPC groups treated with osteogenic differentiation conditions were below 0.01.

Three weeks being the sufficient period for cellular mineral accumulation. Differences in optical density were observed between 2 and 3 weeks. Although osteogenic behaviors were observed for all samples, the capability for osteogenesis of EB/CS-100 was lower than those of the other EB-CPCs. Changes in cellular shapes influenced by surface roughness and surface topography likely affected cell behaviors such as the osteogenesis and proliferation (Fig. 5). The cell shape regulates the stem cell growth

Fig. 5 Schematics of study. EB-CPCs were fabricated with various sized EBPs and CS solution. Larger EBPs led to rougher CPC surfaces, whereas smaller EBPs led to smoother CPC surfaces. Cells on rougher surfaces showed better viability than those on smoother surfaces. With calcium deposition assay, cells on smoother surfaces showed better calcium deposition than those on rougher surfaces. In conclusion, EB-CPCs made by smaller EBPs are appropriate for bone formation, whereas those made by larger EBPs are appropriate for stem cell differentiation



and physiology (Abagnale et al., 2015; Liu et al., 2015; Singhvi et al., 1994). McBeath et al. showed that MSCs have an osteoblastic phenotype (spreading with rounded shapes larger than adipocytes) when they differentiate into osteoblasts (McBeath et al., 2004). Consequently, cells with lower axis ratios exhibited a better osteogenic differentiation capability, whereas those with higher major/minor axis ratios exhibited a better cell growth. In accordance with the results, the surface topographical properties of EB-CPCs can be controlled by the particle size. This will be useful for the design of the mechanical strengths of composites and behaviors of surrounding cells.

Conclusions

The objectives of this study were to develop CPCs with various sizes of EBPs and evaluate their proliferation and osteogenic differentiation abilities. There was no significant difference between FTIR and XRD patterns at different particle sizes of the EBP, which indicates that the milling process did not affect the crystal structure and functional groups. The surface roughness of the EB/CSs was induced by the size of the EBPs. The cell behavior was influenced by the surface roughness of the EB-CPCs. The cell morphologies were strongly influenced by the surface roughness. A higher R_z led to elongated shape, resulting in an enhanced cell proliferation. A lower R_z value led to rounded shape, resulting in an enhanced osteogenic differentiation. EB-CPCs with various sizes will be useful for different bone healing situations.

Supplementary Information The online version contains supplementary material available at <https://doi.org/10.1007/s42853-023-00199-5>.

Author Contribution Conceptualization: K.-J.J., J.K., and J.H.C.; investigation: K.-J.J., S.P., Y.H., and H.S.; resources: K.-J.J., K.-T.L., J.K., and J.H.C.; writing—original draft preparation: K.-J.J., S.P., J.L., and H.S.; visualization: S.P., Y.H., J.L., and H.S.; supervision: K.-J.J. and J.K.; project administration: J.K. and J.H.C.; funding acquisition: K.-J.J. and J.H.C. All authors have read and agreed to the published version of the manuscript.

Funding This work was supported by Korea Institute of Planning and Evaluation for Technology in Food, Agriculture, and Forestry (IPET) through Agri-Bio Industry Technology Development Program funded by the Ministry of Agriculture, Food and Rural Affairs (MAFRA) (116135-3). This work was supported by Korea Institute of Planning and Evaluation for Technology in Food, Agriculture and Forestry (IPET) through Agriculture, Food and Rural Affairs Convergence Technologies Program for Educating Creative Global Leader, funded by Ministry of Agriculture, Food and Rural Affairs (MAFRA) (Project No. 320001-4), Republic of Korea. This work was supported by the Technology development Program(S3125387) funded by the Ministry of SMEs and Startups (MSS, Korea). This research was supported by Basic Science Research Program through the National Research Foundation of Korea (NRF) funded by the Ministry of Education (NRF-2022R111A1A01065625). This work was supported by the Korea Institute of Planning and Evaluation for Technology in Food, Agriculture, and Forestry(IPET) through Agriculture, Food, and Rural Affairs Convergence Technologies Program for Educating Creative Global Leader, funded by the Ministry of Agriculture, Food, and Rural Affairs(MAFRA) (717001-7).

Data Availability All data are available from the corresponding author upon reasonable request.

Declarations


Competing Interests The authors declare no competing interests.

References

- Abagnale, G., Steger, M., Nguyen, V. H., Hersch, N., Sechi, A., Jousen, S., Denecke, B., Merkel, R., Hoffmann, B., & Dreser, A. (2015). Surface topography enhances differentiation of mesenchymal stem cells towards osteogenic and adipogenic lineages. *Biomaterials*, *61*, 316–326. <https://doi.org/10.1016/j.biomaterials.2015.05.030>
- Akram, M., Ahmed, R., Shakir, I., Ibrahim, W. A. W., & Hussain, R. (2014). Extracting hydroxyapatite and its precursors from natural resources. *Journal of Materials Science*, *49*(4), 1461–1475. <https://doi.org/10.1007/s10853-013-7864-x>
- Alkhraisat, M., Rueda, C., Marino, F., Torres, J., Jerez, L., Gbureck, U., & Cabarcos, E. (2009). The effect of hyaluronic acid on brushite cement cohesion. *Acta Biomaterialia*, *5*(8), 3150–3156. <https://doi.org/10.1016/j.actbio.2009.04.001>
- Ambrosio, L., Guarino, V., Sanginario, V., Torricelli, P., Fini, M., Ginebra, M., Planell, J., & Giardino, R. (2012). Injectable calcium-phosphate-based composites for skeletal bone treatments. *Biomedical Materials*, *7*(2), 024113. <https://doi.org/10.1088/1748-6041/7/2/024113>
- Barralet, J. E., Tremayne, M., Lilley, K. J., & Gbureck, U. (2005). Modification of calcium phosphate cement with α -hydroxy acids and their salts. *Chemistry of Materials*, *17*(6), 1313–1319. <https://doi.org/10.1021/cm048803z>
- Bettinger, C. J., Langer, R., & Borenstein, J. T. (2009). Engineering substrate topography at the micro-and nanoscale to control cell function. *Angewandte Chemie International Edition*, *48*(30), 5406–5415. <https://doi.org/10.1002/anie.200805179>
- Bigerelle, M., Anselme, K., Noel, B., Ruderman, I., Hardouin, P., & Iost, A. (2002). Improvement in the morphology of Ti-based surfaces: A new process to increase in vitro human osteoblast response. *Biomaterials*, *23*(7), 1563–1577. [https://doi.org/10.1016/S0142-9612\(01\)00271-X](https://doi.org/10.1016/S0142-9612(01)00271-X)
- Biggs, M. J., Richards, R. G., Gadegaard, N., McMurray, R. J., Affrossman, S., Wilkinson, C. D., Oreffo, R. O., & Dalby, M. J. (2009). Interactions with nanoscale topography: Adhesion quantification and signal transduction in cells of osteogenic and multipotent lineage. *Journal of Biomedical Materials Research Part A: An Official Journal of the Society for Biomaterials, the Japanese Society for Biomaterials, and the Australian Society for Biomaterials and the Korean Society for Biomaterials*, *91*(1), 195–208. <https://doi.org/10.1002/jbm.a.32196>
- Bigi, A., Bracci, B., & Panzavolta, S. (2004). Effect of added gelatin on the properties of calcium phosphate cement. *Biomaterials*, *25*(14), 2893–2899. <https://doi.org/10.1016/j.biomaterials.2003.09.059>
- Böker, D.-K., Schultheiß, R., & Probst, E. M. (1989). Radiologic long-term results after cervical vertebral interbody fusion with polymethyl methacrylat (PMMA). *Neurosurgical Review*, *12*(3), 217–221. <https://doi.org/10.1007/BF01743989>
- Clark, P., Connolly, P., Curtis, A., Dow, J., & Wilkinson, C. (1990). Topographical control of cell behaviour: II. Multiple grooved substrata. *Development*, *108*(4), 635–644. <https://doi.org/10.1242/dev.108.4.635>
- Giannoudis, P. V., Dinopoulos, H., & Tsiridis, E. (2005). Bone substitutes: An update. *Injury*, *36*(3), S20–S27. <https://doi.org/10.1016/j.injury.2005.07.029>
- Hofmann, G., Kirschner, M., Wangemann, T., Falk, C., Mempel, W., & Hammer, C. (1995). Infections and immunological hazards of allogeneic bone transplantation. *Archives of Orthopaedic and Trauma Surgery*, *114*(3), 159–166. <https://doi.org/10.1007/BF00443390>
- Jang, K.-J., Cho, W. J., Seonwoo, H., Kim, J., Lim, K. T., Chung, P.-H., & Chung, J. H. (2014). Development and characterization of horse bone-derived natural calcium phosphate powders. *Journal of Biosystems Engineering*, *39*(2), 122–133. <https://doi.org/10.5307/JBE.2014.39.2.122>
- Jang, K.-J., Seonwoo, H., Yang, M., Park, S., Lim, K. T., Kim, J., Choung, P.-H., & Chung, J. H. (2021). Development and characterization of waste equine bone-derived calcium phosphate cements with human alveolar bone-derived mesenchymal stem cells. *Connective Tissue Research*, *62*(2), 164–175. <https://doi.org/10.1080/03008207.2019.1655003>
- Kim, H.-B., Patel, D. K., Seo, Y.-R., & Lim, K.-T. (2019). 3D-Printed scaffolds with reinforced poly (lactic acid)/carbon nanotube filaments based on melt extrusion. *Journal of Biosystems Engineering*, *44*(2), 120–127. <https://doi.org/10.1007/s42853-019-00011-3>
- Lim, J. W., Jang, K. J., Son, H., Park, S., Kim, J. E., Kim, H. B., Seonwoo, H., Choung, Y. H., Lee, M. C., & Chung, J. H. (2020). Aligned nanofiber-guided bone regeneration barrier incorporated with equine bone-derived hydroxyapatite for alveolar bone regeneration. *Polymers*, *13*(1), 60. <https://doi.org/10.3390/polym13010060>
- Liu, Y.-J., Le Berre, M., Lautenschlaeger, F., Maiuri, P., Callan-Jones, A., Heuzé, M., Takaki, T., Voituriez, R., & Piel, M. (2015). Confinement and low adhesion induce fast amoeboid migration of slow mesenchymal cells. *Cell*, *160*(4), 659–672. <https://doi.org/10.1088/1748-6041/7/2/024113>
- Mahendra, A., & Maclean, A. (2007). Available biological treatments for complex non-unions. *Injury*, *38*, S7–S12. [https://doi.org/10.1016/S0020-1383\(08\)70004-4](https://doi.org/10.1016/S0020-1383(08)70004-4)
- McBeath, R., Pirone, D. M., Nelson, C. M., Bhadriraju, K., & Chen, C. S. (2004). Cell shape, cytoskeletal tension, and RhoA regulate stem cell lineage commitment. *Developmental Cell*, *6*(4), 483–495. [https://doi.org/10.1016/S1534-5807\(04\)00075-9](https://doi.org/10.1016/S1534-5807(04)00075-9)
- Mucalo, M. R., & Worth, A. J. (2008). Biomedical from bone. *Chemistry in New Zealand*, *21*(1), 13–18. <https://hdl.handle.net/10289/3979>
- Park, S., Kim, J. E., Han, J., Jeong, S., Lim, J. W., Lee, M. C., Son, H., Kim, H. B., Choung, Y.-H., & Seonwoo, H. (2021). 3Dprinted poly (ϵ -caprolactone)/hydroxyapatite scaffolds modified with alkaline hydrolysis enhance osteogenesis in vitro. *Polymers*, *13*(2), 257. <https://doi.org/10.3390/polym13020257>
- Ruijtenberg, S., & van den Heuvel, S. (2016). Coordinating cell proliferation and differentiation: Antagonism between cell cycle regulators and cell type-specific gene expression. *Cell Cycle*, *15*(2), 196–212. <https://doi.org/10.1080/15384101.2015.1120925>
- Salamanca, E., Hsu, C.-C., Huang, H.-M., Teng, N.-C., Lin, C.-T., Pan, Y.-H., & Chang, W.-J. (2018). Bone regeneration using a porcine bone substitute collagen composite in vitro and in vivo. *Scientific Reports*, *8*(1), 1–8. <https://doi.org/10.1038/s41598-018-19629-y>
- Shi, Z., Huang, X., Cai, Y., Tang, R., & Yang, D. (2009). Size effect of hydroxyapatite nanoparticles on proliferation and apoptosis of osteoblast-like cells. *Acta Biomaterialia*, *5*(1), 338–345. <https://doi.org/10.1016/j.actbio.2008.07.023>
- Singhvi, R., Kumar, A., Lopez, G. P., Stephanopoulos, G. N., Wang, D. I., Whitesides, G. M., & Ingber, D. E. (1994). Engineering cell shape and function. *Science*, *264*(5159), 696–698. <https://doi.org/10.1126/science.8171320>
- Xu, H., Quinn, J., Takagi, S., & Chow, L. C. (2002). Processing and properties of strong and non-rigid calcium phosphate cement. *Journal of Dental Research*, *81*(3), 219–224. <https://doi.org/10.1177/0810219>
- Xu, H. H., Takagi, S., Quinn, J. B., & Chow, L. C. (2004). Fast-setting calcium phosphate scaffolds with tailored macropore formation rates for bone regeneration. *Journal of Biomedical Materials Research Part A*, *68*(4), 725–734. <https://doi.org/10.1002/jbm.a.20093>
- Zhou, H., & Lee, J. (2011). Nanoscale hydroxyapatite particles for bone tissue engineering. *Acta Biomaterialia*, *7*(7), 2769–2781. <https://doi.org/10.1016/j.actbio.2011.03.019>

Springer Nature or its licensor (e.g. a society or other partner) holds exclusive rights to this article under a publishing agreement with the author(s) or other rightsholder(s); author self-archiving of the accepted manuscript version of this article is solely governed by the terms of such publishing agreement and applicable law.

Authors and Affiliations

Kyoung-Je Jang^{1,2} · Sangbae Park^{3,4,5} · Joo Lee^{6,7} · Yeongeol Hong¹ · Hoon Seonwoo^{7,8} · Ki-Taek Lim⁹ · Jangho Kim^{3,4,5} · Jong Hoon Chung^{10,11,12} 

✉ Jangho Kim
rain2000@jnu.ac.kr

✉ Jong Hoon Chung
jchung@snu.ac.kr

¹ Department of Bio-Systems Engineering, Institute of Smart Farm, Gyeongsang National University, Jinju 52828, Republic of Korea

² Institute of Smart Farm, Gyeongsang National University, Jinju 52828, Republic of Korea

³ Department of Convergence Biosystems Engineering, Chonnam National University, Gwangju 61186, Republic of Korea

⁴ Department of Rural and Biosystems Engineering, Chonnam National University, Gwangju 61186, Republic of Korea

⁵ Interdisciplinary Program in IT-Bio Convergence System, Chonnam National University, Gwangju 61186, Republic of Korea

⁶ Department of Animal Science & Technology, Suncheon National University, Suncheon 57922, Republic of Korea

⁷ Interdisciplinary Program in IT-Bio Convergence System, Suncheon National University, Suncheon 57922, Republic of Korea

⁸ Department of Convergent Biosystems Engineering, College of Life Sciences and Natural Resources, Suncheon National University, Suncheon 57922, Republic of Korea

⁹ Department of Biosystems Engineering, College of Agricultural and Life Sciences, Kangwon National University, Chuncheon 24341, Republic of Korea

¹⁰ Research Institute of Agriculture and Life Sciences, Seoul National University, Seoul 08826, Republic of Korea

¹¹ Department of Biosystems Engineering, Seoul National University, Seoul 08826, Republic of Korea

¹² Convergence Major in Global Smart Farm, College of Agriculture and Life Sciences, Seoul National University, Seoul 08826, Republic of Korea